INVESTIGATION ON MICRO-FLAME STRUCTURE OF AMMONIUM PERCHLORATE COMPOSITE PROPELLANT UNDER WIDE PRESSURE RANGE

by

Kaixuan CHEN[a], Xiaochun XUE[a*], Yonggang YU[a], and Zhenwei YE[b]

[a] School of Energy and Power Engineering, Nanjing University of Science and Technology, Nanjing, Jiangsu, China
[b] School of Science, Hangzhou Dianzi University, Hangzhou, Zhejiang, China

Original scientific paper
https://doi.org/10.2298/TSCI221114054C

This present work proposes a method to exactly evaluate the thermal process of ammonium perchlorate/hydroxyl-terminated polybutadiene propellant. The 3-D propellant pack is generated by the Monte-Carlo method to obtain a representative sandwich model on the base of the dual-slicing technique. The ammonium perchlorate monopropellant flame height H_1, the primary diffusion flame height H_2, and the final diffusion flame height H_3 are jointly determined by the temperature and component distributions of the gas phase thermodynamic field, which is more accurate to capture this complicated combustion field distribution of the gas phase comparing with earlier reported studies. Peclet number and Damkohler number are also introduced to quantitatively investigate the influence mechanism of chemical kinetics and diffusion mixing process of components on this micro-flame structure under wide pressure range (0.69-20.7 MPa). Further, based on the criterion of whether the premixed flow above the burning surface can absorb heat flux continuously from the diffusion flame to approach adiabatic flame temperature, the diffusion flame is divided into two regions in detail: flame front and trailing diffusion flame.

Key words: *AP/HTPB propellant, BDP model, diffusion flame, thermal process*

Introduction

Ammonium perchlorate/hydroxyl-terminated polybutadiene (AP/HTPB) propellant is widely used in the fields of ground launch systems with drag-reduction equipment, solid rocket motors for missiles and rocket launchers due to its high specific impulse, good ignition characteristics, and predictability of the burning rate [1]. However, the combustion process of this composite propellant is very complicated based on the fact that a dispersion of discrete random AP particles in a fuel binder matrix, involving thermal decompositions of multiple solid compositions, gas-solid coupling, premixing and diffusion reactions of gaseous reactants. Further, the premixing and diffusion reactions of combustion gases are particularly affected by the combustion pressure, AP particle size, and binder content. To explore the complex reaction process of the gas zone, Beckstead *et al*. [2] proposed the BDP model, dividing the AP/HTPB combustion process into three coupled flame structures: AP monopropellant flame, primary diffusion flame, and final diffusion flame. Price *et al*. [3] observed the micro-combustion characteristic of composite solid propellant under lower combustion pressure by high speed photography,

* Corresponding author, e-mail: xiaochunxue_njust@163.com

which verified the accuracy of the BDP model. Gross *et al*. [4] developed the BDP model and used a series of modified parameters from the micro-scale model to establish a global dynamic meso-scale combustion model, in which a four-step reaction mechanism was used to describe the gas-flame structure of AP/HTPB propellant.

To describe the reaction of the gas phase more specifically in the combustion process of the AP/HTPB propellant, Buckmaster *et al*. [2] introduced the Peclet number, and Damkohler number, to define the relative size of convective-to-diffusive transport rates as well as the chemical reaction and diffusive transport rates. The values of Peclet number and Damkohler number are closely related to the temperature, species, gas phase heat release rate, burning rate, and other physical quantities. Chorpening [5] further investigated the combustion characteristics of AP/HTPB propellant by adjusting the Peclet number and Damkohler number, which obtained the following conclusions:

– The Peclet number is related to the burning rate and the binder thickness.
– Damkohler number is related to the pressure and the binder thickness.
– Low Peclet number and low Damkohler number make the products of AP and HTPB more fully mixed.

There is a strong correlation between Peclet and Damkohler numbers, and the volume heat release.

To explore the premix and diffusion degree of gaseous reactants in the combustion process of AP/HTPB propellant, the concept of flame height is proposed. It is a comprehensive function of the pressure, AP particle size, and binder content. Beckstead *et al*. [2] pointed out that the AP monopropellant flame and the primary flame are competing for the oxidizing gas in the wide range of pressure. Moreover, since AP/HTPB propellant is heterogeneous in nature with a multi-modal distribution of AP particles embedded in the HTPB polymer matrix, the overall gas flame of AP/HTPB propellant is composed of multiple micro-structure flames. This micro-distribution of heterogeneous AP/HTPB propellant that affected this micro-flame structure can be described by the symmetrical arrangement structure of two AP particles and mutually enwrapped HTPB, which is called the sandwich model. It was first proposed by Powling [6]. The most prominent advantage of the sandwich model is that the flame structure can be observed systematically, which is also the reason why there are so many theoretical studies on the sandwich model [7-10]. Knott and Brewster [11] employed this sandwich model and then selected the Oseen approximation method to eliminate the momentum equation along the x-direction, coupling the gas-solid reaction study the influence of the environment pressure on the flame structure. Chorpening [5] conducted extensive experiments of observing flame structure by ultraviolet emission and transmission imaging 2-D conFiguration of laminae of AP and HTPB, which also verified the numerical results of Knott *et al.* [11].

The importance of solid-phase modelling, especially the reaction of condensed phase, heat transfer, and the distribution of AP particle size has been acknowledged by early models. The approximations with different degrees were also used to simulate real AP/HTPB propellant and then improve computational accuracy and efficiency. Jackson *et al*. [12] first proposed a simplified model that can simulate the internal structure of the composite propellant. Knott *et al*. [13] developed a random particle packing algorithm, which treated AP crystals as disks (2-D) or spheres (3-D). The model was very helpful to simulate the combustion of AP/HTPB propellant, which can be used to obtain the influence of the distribution of AP particles on the burning rate characteristics of this composite propellant. Massa *et al*. [14] examined the combustion process of AP/HTPB propellant by using a simplified three-step reaction mechanism based on this random particle packing algorithm. Vijay *et al*. [15] used X-ray computed

tomography technology to reconstruct the real 3-D AP/HTPB propellant packing and compared it with the random particle packing in the AP exposed area and AP/binder intercept lengths, which confirmed the accuracy of the proposed model used for numerical simulation. However, the solution of the random distribution model needs to consume numerous computational resources. To accurately investigate the burning behaviors of AP/HTPB from the micro level and simplify the calculation requirements, Vijay *et al*. [16] sliced the generated random particle packing to obtain the representative sandwich model and then used it to calculate the burning rate of AP/HTPB propellant. Compared with the experimental data of Miller [17], Ishitha and Ramakrishna [18], and Kubota and Miyazaki [19], the results showed that the model was successful in predicting the burning rate of AP/HTPB propellant.

In this work, the focus is to develop a method to exactly evaluate the micro-AP/HTPB combustion that is generated by the Monte-Carlo method and then intercepted by dual-slicing technology introduced according to Vijay's report [16]. Subsequently, the gas-solid coupling model and the BDP model of AP/HTPB propellant with micro-scale are established and are used to study the micro-components reaction mechanism and heat flow exchange characteristic of this AP/HTPB propellant in a larger range of environment pressure from 0.69-20.7 MPa in more detail by numerical simulation. A comprehensive evaluation method using Peclet number, Damkohler number, and flame heights is proposed quantitatively to explain the chemical kinetics and diffusion mixing process of the gas-phase combustion region of AP/HTPB propellant. Further, the diffusion flame is divided into flame front and trailing diffusion flame based on the criterion of whether the premixed flow above the burning surface can absorb heat flux continuously from the diffusion flame to approach adiabatic flame temperature.

Numerical model

Generation and intercept method of AP/HTPB propellant with a random particle packing

The bridge to represent real AP/HTPB solid propellant by using a representative sandwich is the establishment of the 3-D random model, where the most important process is the selection of AP particle size and number. Since different AP particle sizes are embedded into the HTPB binder, the burning rate and micro-flame structure of AP/HTPB propellant will be significantly affected. Miller [17] used 400 μm, 200 μm, 20 μm, 5μm or even smaller AP particles to synthesize 29 non-aluminized propellants to obtain experimental burning rata data base, providing the data available for comparison with various theoretical models. In this paper, based on Miller's experiment [17], three types of AP/HTPB propellant structures (SD III-16, SD III-22, and SD III-24) with an AP particle loading rate of 86% are established by the Monte-Carlo method. The proportions of different sizes of AP particles and HTPB layer are shown in tab. 1, and the structure is shown in fig. 1, where pink spheres represent 400 μm AP particles, red spheres represent 200 μm AP particles, blue spheres represent 50 μm AP particles, and yellow spheres represent 20 μm AP particles).

Table 1. The Proportion of different particles in AP/HTPB propellant [17]

Composition	Mass fraction of AP [%]				Mass fraction of HTPB [%]
	400 μm	200 μm	50 μm	20 μm	
SD III-16	0	31	31	24	14
SD III-22	31	0	41	14	14
SD III-24	0	31	41	14	14

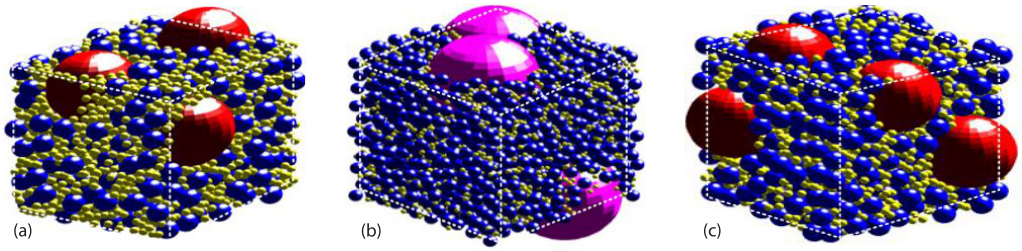

Figure 1. Structure diagram of three types of AP / HTPB propellant; (a) SD III-16, (b) SD III-22, and (c) SD III-24

Using the technique of Vijay and Ramakrishna [16], three kinds of AP/HTPB structures are firstly performed by multiple surface cuttings, as shown in fig. 2, and then 50 planar slices with an interval of 15 μm are generated. Figure 2(b) shows the distribution of AP and HTPB on one of the slices (the circle represents AP particles, and the area not occupied by the AP particles in the slice is the binder in the propellant). Subsequently, 25 linear cuttings with an interval of 30 μm are performed on the generated multi-group slices, that is, a group of parallel lines are used to continuously cut the section. The half intercepts made by the AP particles on the lines are taken as AP particle sizes and the half regions on the line which are not intercepted by AP particles are taken to be the HTPB thickness. Finally, the sizes of AP and HTPB obtained by multiple linear cuttings are averaged, and the relationship between them is obtained, as shown in figs. 2(c) and 2(d). It can be seen from fig. 2 that the HTPB thicknesses of SD III-16, SD III-22, and SD III-24 propellant packages remain stable at 7 μm, 6 μm, and 5 μm after 400 times cutting. After cutting 3500 times, the AP sizes remain steady at 21 μm, 14 μm, and 12μm.

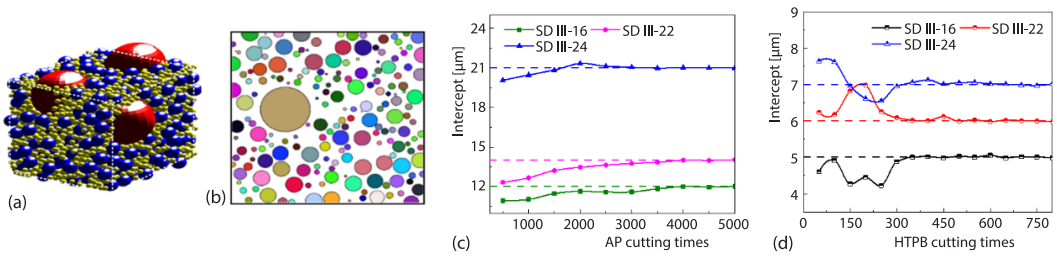

Figure 2. Diagram of cutting method; (a) 3-D AP/HTPB propellant structure, (b) AP/HTPB planar slice, (c) variation curve of AP intercept with cutting times, and (d) variation curve of HTPB intercept with cutting times

However, Vijay and Ramakrishna [16] did not present whether the AP and HTPB intercepts of the sandwich model are necessarily related to the length of the 3-D box. Since the *representative* sandwich model is the micro-structure of the 3-D AP/HTPB propellant, they should have similar combustion characteristics, that is, a *representative* sandwich model represents a kind of AP/HTPB propellant. it is necessary to verify the size independence. Taking SD III-22 propellant as an example, three kinds of propellants with lengths of 800 μm, 900 μm, and 1000 μm are produced and cut according to the aforementioned method. The results are shown in fig. 3. It can be seen from the figure that under the premise of the same AP loading rate and the same proportion of different particle sizes, the intercepts of AP and HTPB keep stable with the change of the 3-D AP/HTPB propellant size. Based on this principle, the *representative* sandwich models of AP/HTPB propellants with three different structures are established, respectively.

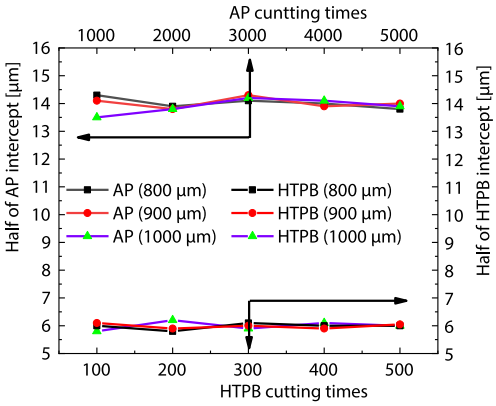

Figure 3. Verification results for size independence

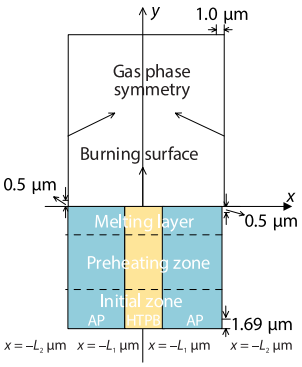

Figure 4. Sanwich model

Physical model

According to the AP and HTPB intercepts in tab. 2, the representative sandwich models of SD III-16, SD III-22, and SD III-24 AP/HTPB propellants are established, as shown in fig. 4. The oxidant AP is located in $L_1 < |x| < L_2$ and the binder HTPB lies in $|x| < L_1$. To simplify the calculation, the following assumptions are proposed:

- Boggs [20] and Hightower and Price [21] found bubbles and ridges exist above the quenched surface of AP, which proved that there was a melting layer near the burning surface, and thus most of the heat flux in the gas phase is transferred to the solid phase by thermal conductivity. To simplify the calculation, thermal feedback only considers the thermal conductivity of the gas relative to the burning surface.
- The oxidant AP and binder HTPB are regarded as two independent components with different thermophysical parameters, the solid phase pyrolysis reaction occurs on the burning surface layer, and only the heat conduction effect is considered in the solid phase.
- Assuming that the gas is the ideal gas and the Lewis number of all components of the gas phase is 1. Moreover, the gas thermal conductivity λ_g is the function of temperature.
- The thermal decomposition of solid propellant is described by zero-order Arrhenius Law, and the gas phase combustion process of AP/HTPB is described by the BDP flame model combined with the two-step global reaction mechanism.
- The pressure is uniformly distributed throughout the gas phase on a micro-scale.

Mathematical model

Chemical kinetic equation

The combustion of AP/HTPB is divided into two processes including the solid phase and the gas phase. The physical and chemical phenomena of the solid phase process include AP and HTPB preheated by heat conduction and endothermic pyrolysis of these two-components, and thus the corresponding solid region is also divided into the solid preheating zone and solid reaction zone. The solid phase reaction zone is located on the solid phase surface, which is the melting layer. The AP component undergoes the following thermal decomposition reactions:

$$\mathrm{AP}(s) \xrightarrow{Q_{c,\mathrm{AP}}} \underbrace{\mathrm{NH_3}(g) + \mathrm{HClO_4}(g)}_{\tilde{X}} \tag{1}$$

The HTPB undergoes the following pyrolysis reaction:

$$\mathrm{HTPB}(s) \xrightarrow{Q_{c,\mathrm{B}}} \underbrace{C_2\mathrm{H}_4(g)}_{\tilde{Y}} \tag{2}$$

where the formula of eq. (1) is an exothermic reaction, the decomposition heat is expressed as $Q_{c,\mathrm{AP}}$, eq. (2) is an endothermic reaction, the decomposition heat is expressed as $Q_{c,B}$.

Zero-order Arrhenius law was used to describe the pyrolysis rates of two solid components:

$$\dot{m}_{\mathrm{AP}} = \rho_{\mathrm{AP}} A_{\mathrm{AP}} \exp\left(\frac{-E_{\mathrm{AP}}}{\mathrm{R}_u T_{\mathrm{AP},S}}\right) \tag{3}$$

$$\dot{m}_{\mathrm{B}} = \rho_{\mathrm{B}} A_{\mathrm{B}} \exp\left(-\frac{E_{\mathrm{B}}}{\mathrm{R}_u T_{\mathrm{B},S}}\right) \tag{4}$$

where ρ_{AP} and ρ_{B} are the density of oxidant AP and binder HTPB, A_{AP} and A_{B} – the pyrolysis rate constants, E_{AP} and E_{B} are pyrolysis activation energy of oxidant AP and binder HTPB, respectively, T_{AP}, S, and T_{B}, S – the burning surface temperature of oxidant AP and binder HTPB, and $\mathrm{R_u}$ is the general gas constant.

The pyrolysis products of the solid phase are used as the reactant of the gas phase process, and the two-step global reaction mechanism based on BDP multi-flame model is used to describe the combustion process of the gas phase reaction:

$$\underbrace{\mathrm{NH_3}(g) + \mathrm{HClO_4}(g)}_{\tilde{X}} \xrightarrow{R_1} \underbrace{\mathrm{O_2}(g) + \mathrm{H_2O}(g) + \mathrm{HCl}(g) + \mathrm{N_2}(g)}_{\tilde{Z}} \tag{5}$$

$$\underbrace{\mathrm{C_2H_4}}_{\tilde{X}} + \beta\left(\underbrace{\mathrm{O_2}(g) + \mathrm{H_2O}(g) + \mathrm{HCl}(g) + \mathrm{N_2}(g)}_{\tilde{Z}}\right) \xrightarrow{R_2} \underbrace{\mathrm{CO_2}(g) + \mathrm{H_2O}(g) + \mathrm{HCl}(g) + \mathrm{N_2}(g)}_{\text{final productus}} \tag{6}$$

where component $\tilde{X}$ is the $\mathrm{NH_3}$ (g) + $\mathrm{HClO_4}$ (g), omponent $\tilde{Y}$ on behalf of $\mathrm{C_2H_4}$, component $\tilde{Z}$ – $\mathrm{H_2O}$ (g) + HCl (g) + $\mathrm{O_2}$ (g) + $\mathrm{N_2}$ (g), respectively, β – the AP mass required to consume 1 kg HTPB, and the Arrhenius law is employed to describe chemical reaction rates R_1 and R_2:

$$R_1 = D_1 P^{n_1} [X] \exp\left(-\frac{E_1}{\mathrm{R_u} T}\right) \tag{7}$$

$$R_2 = D_2 P^{n_2} [Y][Z] \exp\left(-\frac{E_2}{\mathrm{R}_u T}\right) \tag{8}$$

where D_1 and D_2 are pre-exponential factors, n_1 and n_2 – the pressure indexes, E_1 and E_2 – the reaction activation energy, respectively, [X], [Y], and [Z] – the mass fractions of components $\tilde{X}$, $\tilde{Y}$, and $\tilde{Z}$, and subscripts 1 and 2 correspond to the first step and the second step reaction.

Solid-phase equation

The solid phase only considers the thermal conduction process and is expressed:

$$\rho_c c_c \frac{\partial T}{\partial t} = \frac{\partial}{\partial y}\left(\lambda_c \frac{\partial T}{\partial y}\right) + \frac{\partial}{\partial x}\left(\lambda_c \frac{\partial T}{\partial x}\right) + s_c \tag{9}$$

where ρ_c, c_c, λ_c, and sc are density, specific heat, thermal conductivity, and energy source term of solid phase, respectively:

$$\lambda_c = \begin{cases} \lambda_{\mathrm{B}} \\ \lambda_{\mathrm{AP}} \end{cases},\ \rho_c = \begin{cases} \rho_{\mathrm{B}} \\ \rho_{\mathrm{AP}} \end{cases},\ c_c = \begin{cases} c_{\mathrm{B}}, & |x| < L_1 \\ c_{\mathrm{AP}}, L_1 < |x| < L_2 \end{cases}$$

Gas-phase equation

The multi-component Navier-stokes equation in the plane rectangular co-ordinate system is established for the gas phase.

Continuity equation:

$$\frac{\partial \rho_g}{\partial t} + \nabla\left(\rho_g \vec{\mathrm{V}}\right) = S_{\mathrm{m}} \tag{10}$$

Momentum equation:

$$\frac{\partial\left(\rho_g \vec{\mathrm{V}}\right)}{\partial t} + \nabla\left(\rho_g \vec{\mathrm{V}}\vec{\mathrm{V}}\right) = -\nabla p + \frac{1}{3}\nabla\left(\mu_g \nabla \vec{\mathrm{V}}\right) + \Delta\left(\mu_g \vec{\mathrm{V}}\right) + S_{\mathrm{mom}} \tag{11}$$

Components equation:

$$\rho_g\left(u\frac{\partial Y_i}{\partial X} + v\frac{\partial Y_i}{\partial y}\right) = \nabla\left(\rho_g D_{Y,i}\nabla Y_i\right) + S_i \tag{12}$$

Energy equation:

$$\rho_g C_p\left(u\frac{\partial T}{\partial x} + v\frac{\partial T}{\partial y}\right) = \nabla\left(\lambda_g \nabla T\right) + S_{\mathrm{eng}} \tag{13}$$

State equation:

$$\rho_g \mathrm{R}_u T = pM_u \tag{14}$$

where ρ_g, μ_g, c_p, λ_g and M_u are the density, viscosity coefficient, constant pressure specific heat capacity, thermal conductivity, and molecular molar weight of the gas, $D_{Y,i}$ is the binary diffusion coefficient of one of the components in the mixture, R_u – the general gas constant, Y_i – the mass fraction of the components, $\vec{\mathrm{V}} = (\vec{\mathrm{u}}, \vec{\mathrm{v}})$, and $\vec{\mathrm{u}}$ and $\vec{\mathrm{v}}$ are velocity components along the x- and y-directions, respectively, S_{m}, S_{mom}, S_i, and S_{eng} are the terms of mass source, momentum source, component source, and energy source.

The thermal conductivity λ_g of gas is the function of temperature T:

$$\lambda_g = 1.08 \cdot 10^{-4} T + 0.0133 \tag{15}$$

The gas viscosity μ_g is the function of the thermal conductivity λ_g:

$$\mu_g = \frac{\mathrm{Pr}\lambda_g}{C_p} \tag{16}$$

Equivalent source term method

Assuming that the phase transition occurs in a thin layer of the burning surface, the source terms are added into this layer of the grid to represent the mass-flow of the burning surface, namely:

$$\dot{m} = \rho_c r_b \tag{17}$$

where

$$r_b = \begin{cases} r_{\mathrm{B}} = A_{\mathrm{B}} \exp\left(-\dfrac{E_{\mathrm{B}}}{\mathrm{R_u} T_s}\right) & |x| < L_1 \\ r_{\mathrm{AP}} = A_{\mathrm{AP}} \exp\left(-\dfrac{E_{\mathrm{AP}}}{\mathrm{R_u} T_s}\right) & L_1 < |x| < L_2 \end{cases}$$

To ensure the continuity of the burning rate at the AP/HTPB interface, the burning rate at the interface of two-components of solid is modified by the method of [22]:

$$r_b = r_{\mathrm{B}}^{0.25} r_{\mathrm{AP}}^{0.75} \tag{18}$$

The corresponding gas mass source, momentum source, energy source, component $\tilde{X}$ source, component $\tilde{Y}$ source, and component $\tilde{Z}$ source terms can be expressed:

$$\begin{pmatrix} S_{\mathrm{m}} \\ S_{\mathrm{mom}} \\ S_{\mathrm{eng}} \\ S_{\tilde{X}} \\ S_{\tilde{Y}} \\ S_{\tilde{Z}} \end{pmatrix} = \begin{pmatrix} \dfrac{\rho_c r_b}{\Delta y} \\ \dfrac{\rho_c r_b \vec{\mathrm{V}}}{\Delta y} \\ \sum Q_{g,i} R_i \\ -R_1 \\ -R_2 \\ R_1 - \beta R_2 \end{pmatrix} \tag{19}$$

where Δy is the grid length of the combustion surface layer, R_i and $Q_{g,i}$ are the reaction heat and reaction rate of step i (namely, R_i represents R_1 and R_2).

The energy source terms of oxidant AP and binder HTPB can be expressed:

$$\begin{pmatrix} S_{c,\mathrm{AP}} \\ S_{\mathrm{B}} \end{pmatrix} = \begin{pmatrix} \dfrac{\rho_{\mathrm{AP}} r_b Q_{c,\mathrm{AP}}}{\Delta y} \\ \dfrac{\rho_{\mathrm{B}} r_b Q_{c,\mathrm{B}}}{\Delta y} \end{pmatrix} \tag{20}$$

Gas-phase coupling relationship

In the combustion process, the gas-solid interface temperature keeps continuous, namely:

$$T\big|_{y=0^+} = T\big|_{y=0^-} \tag{21}$$

where 0 is the burning surface, 0^+ – the gas phase side of the burning surface, and 0^- – the solid phase side of the burning surface.

The mass flux on the burning surface remains balanced, namely:

$$\rho_g V_g = \rho_c r_b \tag{22}$$

where V_g is the gas velocity.

The components balance at the burning surface can be expressed:

$$\dot{m}\ Y_i\big|_{y=0^+} - \rho_g D_Y \left.\frac{\partial Y_i}{\partial y}\right|_{y=0^+} = \dot{m}\, Y_i\big|_{y=0^-} \tag{23}$$

where D_Y is the average binary diffusion coefficient of gas.

The heat flux balance at the burning surface can be expressed:

$$\lambda_g \left.\frac{\partial T_g}{\partial y}\right|_{y=0^+} + \rho_c r_b Q_c = \lambda_c \left.\frac{\partial T_c}{\partial y}\right|_{y=0^-} \tag{24}$$

Boundary conditions and calculation methods

Because the left and right boundaries are symmetrical, only half of the region, that is, the part of model $x > 0$ μm, is calculated. The axial length of the solid phase is 500 μm, and the axial length of the gas phase is 700 μm. There are the following boundary conditions for the solid-phase far field, gas-phase far field, and symmetric boundary.

The far field of the solid phase:

$$T\big|_{y=-\infty} = 300K \tag{25}$$

The far field of the gas phase:

$$\left.\frac{\partial Y_i}{\partial y}\right|_{y=+\infty} = 0 \quad Y_i = T, \tilde{X}, \tilde{Y}, \tilde{Z} \tag{26}$$

Symmetric boundary:

$$\left.\frac{\partial F}{\partial x}\right|_{x=0,\pm L_2} = 0 \quad F = \vec{\mathrm{u}}, \vec{\mathrm{v}}, T, \tilde{X}, \tilde{Y}, \tilde{Z} \tag{27}$$

The boundary conditions of gas-solid interface:

$$Y_{\tilde{X}} = 0,\ Y_{\tilde{Y}} = 1,\ Y_{\tilde{Z}} = 0 \quad |x| < L_1 \tag{28}$$

$$Y_{\tilde{X}} = 1,\ Y_{\tilde{Y}} = 0,\ Y_{\tilde{Z}} = 0, \quad L_1 < |x| < L_2 \tag{29}$$

After the grid independence test, the grid division method is determined the grid size is 0.5 μm by using uniform grid division along the x-direction. The gas phase and solid phase regions along the y-direction adopt the tapered grid, where the minimum grid size with 0.5 μm is located in both sides of the burning surface and the maximum grid size with 1.69 μm is located in the far field of gas phase and solid phase. At the same time, the numerical calculation is carried out based on the finite volume method. The pressure-velocity coupling adopts the SIMPLE scheme, and the density, mass, momentum, and component equations adopted the second-order upwind scheme. The physical parameters can be seen in [22].

Validation of the calculation model

As can be seen from fig. 5, the calculated average burning rates of SD III-16 and SD III-22 are in reasonable agreement with experimental results, and the average errors calculated by eq. (30) are 2.43% and 7.01%. The calculated burning rates of SD III-24 under high pressure conditions deviate slightly from experimental values, and the average error is 10.0%. Vijay and Ramakrishna [16], Kumar *et al.* [23], and Kumar and Mukundu [24] pointed out that the density and temperature sensitivity of propellant also affected the burning rate, which is rarely reported in previous literature. It is a possible reason cause a deviation between the calculation results and the experiment reported results:

$$\text{Mean absolute percentage error} = \frac{1}{m}\sum_{i=1}^{m}\left|\frac{pre_i - Ac_i}{Ac_i}\right| \tag{30}$$

where $r_b(x, y, z)$ is the local burning rate, $\overline{r}_b$ – the average burning rate, and A – the burning surface area. The pre_i represents the calculated value, Ac_i is the experimental value, and m represents the number of local burning rate points.

The burning rate plays an important role to characterize the performance of the rocket engine and ground launch vehicle, the relationship between the burning rate and the propellant working pressure satisfies an exponential relation:

$$\overline{r}_b = ap^n \tag{31}$$

where the constant a is the burning rate at unit pressure, and the constant n is the pressure index. By fitting the average burning rate curves of AP/HTPB with different structures under different pressures in fig. 5(d), the values of a and n in eq. (33) are obtained as shown in tab. 2, which is consistent with the AP/HTPB pressure index in the range of 0.4-0.6 given in [11].

Table 2. Temperature coefficient and pressure index

Case	Burning rate at unit pressure, a	Pressure exponent, n
SD III-16	0.596	0.448
SD III-22	0.529	0.481
SD III-24	0.498	0.457

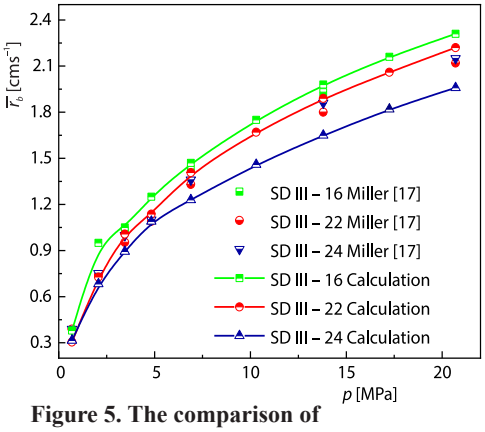

Figure 5. The comparison of average burning rate

Effect of environment pressure on the micro-combustion characteristic

Gas-phase heat release rate of the micro-combustion field

Heat release is a proportional measurement of the reaction strength and flame structure in the gas phase. Figure 6 shows the contours of the gas-phase heat release rate under different environmental pressures for SD III-22 AP/HTPB propellant. When the environment pressure is 0.69 MPa, the reaction rate is slow. Thus, components $\tilde{Y}$ and $\tilde{Z}$ have sufficient time to mix. Compared with high pressure conditions, the core of the heat release rate is larger and far away from the burning surface. As the pressure increases, the core area of the gas-phase heat release rate decreases and moves towards the AP/HTPB interface. At the same time, the diffusion flame develops continuously, and two bands of independent diffusion flame are gradually formed. Chorpening [5] found that the micro-flames with 120-160 μm sandwich propellants were separated through the experiments when the pressure reached to 3.2 MPa. The representative sandwich model used in this paper is only 20 μm, and the flame shows a stronger premixed effect. So, the flame separation occurs delayed. When the pressure rises

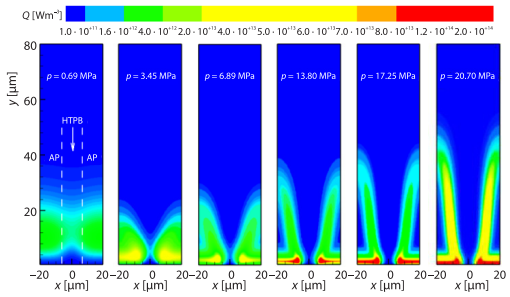

Figure 6. Gas-phase heat release rate under different pressures for SD III-22

to 13.8 MPa or above, the AP monopropellant flame moves closer to the burning surface while the final diffusion flame becomes taller and more concentrated along the stoichiometric surface.

An increase in pressure increases the gas-phase energy production rate, this in turn influences the heat flux to the AP/HTPB propellant. The burning surface thermal feedback profiles, fig. 7, demonstrate how the overall heat flux to the solid phase become under different pressures. It can be seen that the thermal feedback distribution of the whole burning surface is relatively balanced under low pressure condition. With an increase of the operating pressure, the thermal feedback of the AP side is significantly higher than that of the HTPB side, which is consistent with the experimental results of Price *et al*. [3]. At the same time, there is an increasingly peak near the AP/HTPB interface. This because only the species near the oxidizer fuel interface can fully react and produce more combustion heat. Taking the simulation of 13.8 MPa as an example, the peak value of this heat feedback is 138.37 Wm^{-2}, the thermal conductivity at the center of AP is 95.6 Wm^{-2}, and the heat flux at the center of HTPB is 27.20 Wm^{-2}. That is to say, the maximum heat feedback of the burning surface under this environment pressure is 1.48 times and 5.08 times than that above AP and HTPB, which is also the main reason that the local burning rate of AP is greater than that of HTPB.

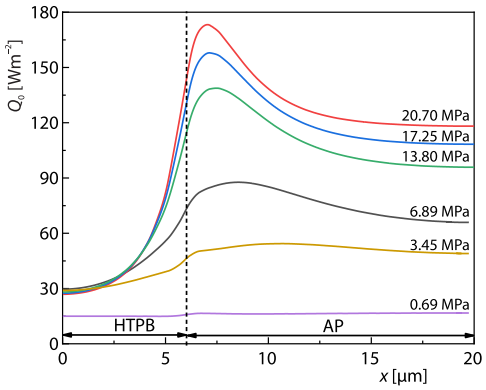

Figure 7. Thermal feedback distribution under wide pressure range

The predicted temperature profiles of the micro-combustion field under different ambient pressures are shown in fig. 8. To examine various combustion characteristics of the micro-flame structure of AP/HTPB propellant, the angle β of 2420 K temperature contour above the oxidizer fuel interface is introduced to analyze temperature distribution characteristics of the gas phase, β are calculated as 107° for 3.45 MPa, 63° for 6.89 MPa 26° for 13.8 MPa 20° for 17.25 MPa and 15° for 20.7 MPa, respectively. The reason for the variation of β is explained as: the diffusion length scale at a certain binder width is determined by the ambient pressure. As environmental pressure increases, the species from the oxidizer and fuel mix incompletely before reacting. Therefore, a non-dense reaction zone formed in the vicinity of the HTPB surface. This results in the gas temperature gradually changing from uniform to *W*-type distribution, so an increase in pressure decreases the value of β. This trend gives an indirect proof reference [5, 25] reported the splitting of the base of the flame structure as well as the numerical result of fig. 6.

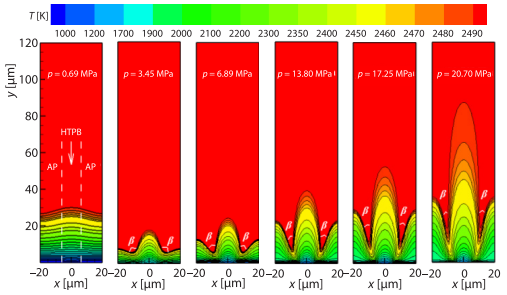

Figure 8. Gas-phase temperature distribution with different pressures for SD III-22

Effects of environment pressure on combustion components $\tilde{X}$ and $\tilde{Z}$

The distribution of components $\tilde{X}$ and $\tilde{Z}$ under different pressures are shown in fig. 8. It can be seen from the fig. 9 that component $\tilde{X}$ is mainly distributed above AP. Its dis-

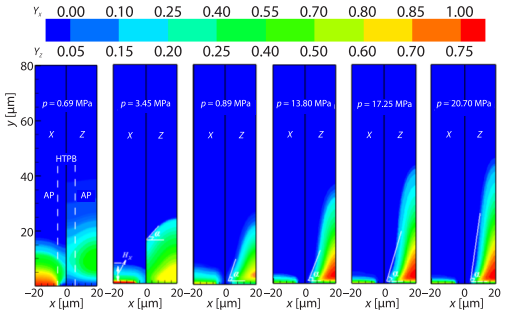

Figure 9. Components $\tilde{X}$ and $\tilde{Z}$ distributions of SD III-22 under different pressures

tribution area decreases considerably with an increase in ambient pressure from 0.69 MPa to 20.7 MPa.When the pressure is 3.45 MPa, the height of the zone H_X where component $\tilde{X}$ content is greater than 0.01 above the AP center is 7.2 μm. When the pressure is 20.7 MPa, H_X is only 2.5 μm. This is because the reduction characteristic time for species reactions makes the consumption of component $\tilde{x}$ easier in the reaction step, R_1, the predicted trend of component $\tilde{X}$ is consistent with the BDP model [2].

Since component $\tilde{Z}$ is both the product of AP decomposition reaction R_1 and the reactant of diffusion-reaction R_2, the influence of chemical reaction and diffusion process on micro-combustion characteristic can be further explained by analyzing the distribution characteristic of component $\tilde{Z}$. When the environment pressure is 0.69 MPa, the distribution core of component $\tilde{Z}$ is slightly away from the burning surface. Its homogeneous distribution and the low content indicate that fuel vapors and oxidizer steam can fully diffuse and mix in the reaction R_2. With the increase in pressure, larger areas are seen to be at higher gas phase heat release, which facilitates the second step of the reaction, R_2. The angle α of the contour where the content of component $\tilde{Z}$ above AP is 0.01 along the $+x$ is 68° for 6.89 MPa. As the ambient rises to 20.7 MPa, α is 82°. The larger and larger region of activity of component $\tilde{Z}$ becomes more difficult for component $\tilde{Y}$ to diffuse into the steam above AP. At the same time, when ambient pressure is 6.89 MPa or above, nearly all of component $\tilde{Z}$ concentrate on the AP side, in accordance with the predicted flame separation phenomenon given in fig. 6.

Effects of environment pressure on micro-flame heights

As mentioned previously, the micro-combustion flame structure of AP/HTPB propellant is very complex, so the concept of flame height is introduced to explore the influences of environmental pressure on its flame structure. Hedmon and co-workers [26, 27] applied high speed planar laser-induced fluorescence to measure diffusion flame formed by different types of propellant. However, there is some uncertainty (*i.e.*, surface compositional fluctuations and irregularities in the measurement process) in measuring the flame height during the experiments; on the other hand, since the AP monopropellant flame length scales are very short, it is difficult to measure its height due to insufficient spatial resolution. Accurate numerical models are needed to capture more details on flame, which benefits the development of new measurement techniques. Zhou *et al*. [28] developed a model for investigating the variation of flame height with pressure from the point of temperature, but they ignored the effect of species on flame structure, thus limiting their work. In this paper, a method is proposed to define different flame heights by the temperature distribution T_1, component $\tilde{X}$ distribution Y_1, and component $\tilde{Z}$ distribution Y_3 along the central axis of the combustion field above the AP surface as well as the axial temperature distribution T_2 and component $\tilde{Z}$ distribution Y_2 along the gas field.

Figure 10 shows the profile of the above physical quantities of SD III-22 AP/HTPB propellant at 6.89 MPa. When T_1 reaches 1400 K [2, 6], the distance from the burning surface is the AP monopropellant flame height, which is expressed as H_1. When T_2 reaches 95% of the adiabatic flame temperature under this condition and Y_2 is less than 0.1%, the distance from the burning surface is the primary diffusion flame height, which is expressed as H_2. When T_1

reaches 99.5% of the adiabatic flame temperature under this condition and Y_3 is less than 0.1%, the distance from the burning surface is the final diffusion flame height, which is represented as H_3. According to the above definition, these flame heights at 6.89 MPa have been marked in fig. 10, which are 1.09 μm, 8.29 μm, and 26.00 μm, respectively.

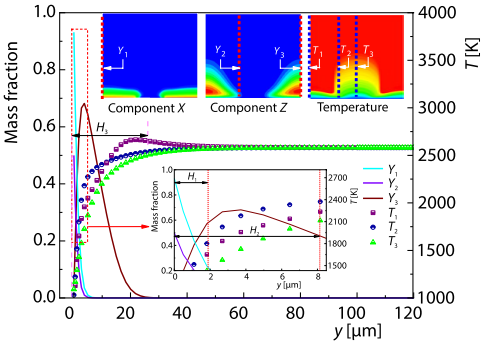

Figure 10. Distribution of component $\tilde{X}$, component $\tilde{Z}$, and temperature

According to the aforementioned method, tab. 3 shows the heights of three kinds of flame structures of AP/HTPB under different pressures. It can be seen that the heights of the primary diffusion flame and final diffusion flame of SD III-24 propellant are significantly higher than those of SD III-16 and SD III-22 under the same pressure conditions. This is because the intercept sizes of AP and HTPB of SD III-24 are relatively large, especially the AP as oxidant is much larger than others. Therefore, for the diffusion reaction R_2, though the fuel component $\tilde{Y}$ increases, the combustion is still in the oxygen-rich environment, forming a higher primary diffusion flame and final diffusion flame. On the base of the fact affected by the physical properties of AP particles, the height of AP monopropellant flame and the content of $\tilde{Y}_1$ are approximately equal for different propellants. Besides, it can be found that H1 decreases and H_3 increases with an increase in pressure. For comparison, fig. 4 of [5] shows AP/HTPB emission images for constant binder thickness of 120-160 μm with varying pressure. As pressure increases, the result shows that the overall diffusion flame appears to be widened and taller, which is consistent with tab. 3 as well as the Shvab-Zeldovich theory in [29]. It also shows the rationality of using temperature and components to jointly define the flame height. However, H_2 shows a downward trend at 0.69-10.3 MPa and remains unchanged at 13.8-20.7 MPa.

Table 3. Heights of micro-flame structures of different AP/HTPB propellants

Parameters	SD III-16				SD III-22				SD III-24				
	H_1	Y_1	H_2	H_3	H_1	Y_1	H_2	H_3	H_1	Y_1	H_2	H_3	
0.69 MPa	4.29	0.60	18.40	–	4.06	0.56	17.95	–	3.84	0.58	19.86	–	I
2.07 MPa	1.74	0.56	9.80	23.50	1.69	0.59	10.04	22.00	1.84	0.56	13.05	37.00	
3.45 MPa	1.32	0.53	8.06	19.90	1.39	0.52	8.97	22.50	1.62	0.48	12.54	39.00	II
4.83 MPa	1.17	0.49	7.74	20.20	1.22	0.48	8.16	21.00	1.43	0.45	12.96	43.00	
6.89 MPa	1.04	0.44	7.20	21.50	1.09	0.41	8.29	26.00	1.23	0.45	13.73	50.70	
10.30 MPa	0.94	0.40	7.30	25.50	0.96	0.39	8.67	31.00	1.02	0.38	13.68	73.00	
13.80 MPa	0.86	0.36	7.69	29.00	0.88	0.36	9.13	37.50	0.92	0.35	16.24	118.93	III
17.25 MPa	0.82	0.33	8.49	33.00	0.83	0.33	10.33	47.30	0.85	0.32	16.70	125.74	
20.70 MPa	0.78	0.31	8.16	38.00	0.79	0.31	9.86	53.50	0.81	0.30	17.02	143.00	

According to the variation of flame heights under different pressures, the pressure range of 0.69-20.7 MPa is divided into three regions. Taking SD III-22 AP/HTPB propellant as an example, the interval of 0.69-2.07 MPa is defined as Region I, where the variation rates of H_1 and H_2 in this region are –1.85 μm/MPa and –6.23 μm/MPa, respectively. The interval of 3.45-10.3 MPa is defined as Region II, where the variation rates of H_1, H_2, and H_3 are

–0.06 μm/MPa, –0.04 μm/MPa, and 1.24 μm/MPa, respectively. The range of 13.8-20.7 MPa is defined as Region III, where the variation rates of H_1, H_2, and H_3 are –0.01 μm/MPa, 0.1 μm/MPa, and 2.32 μm/MPa, respectively. According to the variation rates of flame height above, the variations of H_1 and H_2 are the largest in Region I and the changes in Regions II and III are smaller, indicating that the AP monopropellant flame and the primary diffusion flame are close to the burning surface under high pressure. The variation rate of H_3 also increases with a growth of the pressure, demonstrating that the final diffusion flame controls the gas-phase combustion process of AP/HTPB propellant under high pressure conditions.

Effects of environment pressure on micro-flame structures

To further reveal the influence of different environmental pressures on the micro-flame, three kinds of characteristic time constants, namely characteristic diffusional time T_d, characteristic chemical time T_c, and characteristic flow retention time T_f, are introduced to describe the gas-phase combustion characteristics under different pressure conditions. With the increase of pressure, the chemical reaction time becomes shorter, and the diffusion process gradually becomes the dominant factor affecting the flame structure. Beckstead *et al.* [2] gave the expression of T_d, namely:

$$T_d = \frac{L^2}{D} \tag{33}$$

where L is the scale of the representative sandwich model and D – the mass diffusion coefficient, where $D \propto T^{1.75}/p$.

At the same time, with the increase in pressure, the chemical reaction rate and the gas-flow rate increase. The characteristic chemical time T_c and characteristic flow retention time T_f are described:

$$T_c = \frac{\rho_g}{D_2\, p^{1.7}} \tag{34}$$

$$T_f = \frac{L\rho_g}{\dot{m}} \tag{35}$$

where D_2 is the constant of the R_2 chemical reaction rate, p – the gas pressure, and $\dot{m}$ – the mass-flow on the burning surface.

Figure 11 shows these three kinds of time scales of SD III-22 AP/HTPB propellant micro-combustion with the change of environment pressure. It can be seen that with an increase in the pressure, T_d and T_f increase linearly, while T_c decreases rapidly. When the environment pressure is in the range of 0.69-2.07 MPa, T_c decreases rapidly from $79.0 \cdot 10^{-9}$ $33.8 \cdot 10^{-9}$ second, the diffusion time scale T_d increases from $1.6 \cdot 10^{-5}$-$4.2 \cdot 10^{-5}$ second, and T_f increases from $1.2 \cdot 10^{-4}$-$1.4 \cdot 10^{-4}$ second. The large change rate of T_c forms the dramatic changes of H_1 and H_2 in Region I. When the environment pressure is in the range of 3.45-10.3 MPa, the change rates of T_c, T_d, and T_f are $1.85 \cdot 10^{-9}$ second/MPa, $1.7 \cdot 10$–5 second/MPa, and $1.6 \cdot 10^{-5}$ second/MPa, respectively. Combined with tab. 5, it can be seen that the change rate of T_c in this interval is not very large, so H_1 and H_2 of Region II are unchanged. At the same time, the large variation rates of T_d and T_f indicate that the diffusion mixing rates of combustion gases decrease greatly and the final diffusion flame begins to dominate the micro-combustion process of AP/HTPB. The values of T_c at 0.69 MPa are 9.65 times at 13.8 MPa, 11.35 times at 17.25 MPa, and 12.97 times at 20.7 MPa, respectively. At the same time, the variation rates of T_d and T_f are $1.6 \cdot 10^{-5}$ second/MPa and

$1.2 \cdot 10^{-5}$ second/MPa, which are much larger than T_c. On the one hand, the chemical reaction rate of Region III is getting faster and faster. On the other hand, the variation rates of T_d and T_f with a higher value make the diffusion mixing rates of components $\tilde{Y}$ and $\tilde{Z}$ far behind the chemical reaction rate of R_2, so the change rate of H_3 of the final diffusion flame in Region III is the largest.

Peclet and Damkohler numbers are introduced to represent the relative size of characteristic diffusional time T_d, characteristic chemical time T_c and characteristic flow retention time T_f, where Pe = T_d/T_f and Da = T_d/T_c, as shown in fig. 11. Peclet, which represents the ratio of convective-to-diffusive transport rates, is physically related to the burning rate and the binder thickness. Damkohler number, which represents the ratio of chemical reaction and diffusive transport rates, is related to the pressure and binder thickness. These two parameters are not independent, it can be seen from fig. 12, with an increase in pressure. Peclet and Damkohler numbers all show an increasing trend. Under low pressure condition (0.69-2.07 MPa), it shows $0.126 < \text{Pe} < 0.28$ and $2.0^3 \cdot 10^2 < \text{Da} < 1.24 \cdot 10^3$. The increased diffusion mixing at small Peclet and Damkohler numbers will reduce the local component $\tilde{Y}$ fraction in the overall flame region, which possibly eliminates the presence of stoichiometric regions. In addition, the influence of Damkohler number becomes more subtle compared with Peclet number, affecting reaction intensity. A smallDamkohler number tends to form the *lifted flame* reported in [29] as well as the flame structure that is like that at 0.69 MPa in fig. 15. With an increase of the pressure (2.07-10.3 MPa), it presents $0.28 < \text{Pe} < 0.64$ and $1.24 \cdot 10^3 < \text{Da} < 1.77 \cdot 10^4$. Damkohler number is significantly larger and Peclet number is also continuing to grow in this region, the gas flame gradually attaches to the surface despite the relatively strong convection. The mixture flow begins to move away from the burning surface, in [5, 29] and numerical calculation indicate that fewer oxidizing-gas (component $\tilde{Z}$) reaches the center of HTPB, thus the relatively slow reaction above HTPB causes the separation of flame. In Region II, the micro-combustion process is affected by both chemical kinetics and limited fluid dynamics. The flame shows premixed-diffusion characteristic, forming the flame structure that is like that at 3.45 MPa in fig. 12. When the pressure is above 10.3 MPa ($0.64 < \text{Pe} < 0.86$ and $1.77 \cdot 10^4 < \text{Da} < 5.75 \cdot 10^4$). The reactants are further carried out away from the burning surface because the diffusion process becomes important even dominant, leading to a taller overall diffusion flame concentrated in the AP side, which is like the flame at 20.7 MPa in fig. 12. All in all, the predicted trend of flame structure with Peclet and Damkohler numbers in accordance with BDP model [2], experiment results of [5, 29] and numerical result of this paper.

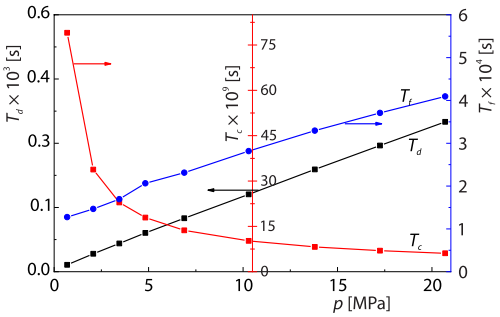

Figure 11. Characteristic parameters of three propellants under different pressures

To further illustrate the effects of the reactants diffusion process on flame structure, the diffusion flame can be divided into two regions by leading edge flame (LEF) [30]:

– flame front and
– trailing diffusion flame.

Based on the aforementioned analysis in this paper, the interaction between diffusion mixing and chemical reaction in the gas phase of AP/HTPB combustion and the resulting flame structure can be further illustrated. That is, near the AP/HTPB burning surface, the diffusion rate between solid pyrolysis products is much faster than the chemical reaction rate due to the low

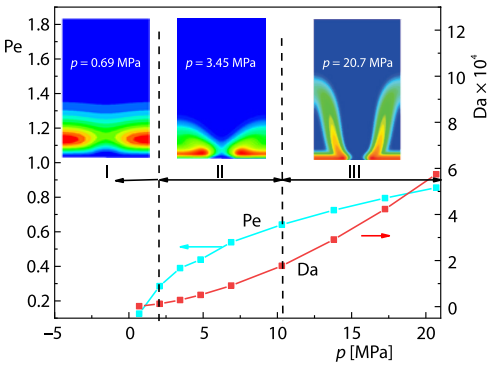

Figure 12. Peclet and Damkohler numbers of SD III-22 AP/HTP

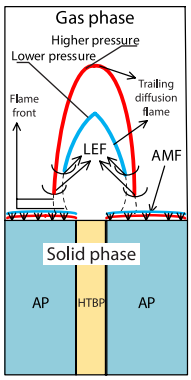

Figure 13. Micro-flame structures

temperature around the burning surface. Thus, a small region of partially premixed reactant flow develops and moves away from the burning surface under the diffusion effect, which continuously absorbs the energy from the high temperature diffusion flame, resulting in a continuous increase in temperature. When the temperature of the premixed reactant flow approaches adiabatic flame temperature, LEF is formed, as shown in fig. 13.

The flame front is located in the gas-flow where the premixed process is concentrated. The chemical reactions occur in this area, which consumes most of the gaseous reactants in the space and yields a lot of heat energy, so the gas-phase heat release core is formed in the flame front. At the same time, the larger heat release causes that the temperature of the gas mixture downstream of the LEF increases rapidly, which becomes a flame holding site for the trailing diffusion flame. Compared with the flame front, the energy of the trailing diffusion flame is lower, which is attributed to the small conductive and convective heat losses in the trailing diffusion flame.

Therefore, when the pressure is low, and Peclet and Damkohler numbers are small, the gas-phase combustion is dominated by chemical kinetics. Due to the lower gas phase release, the premixed flow near the burning surface needs to absorb more energy from the diffusion flame to approach adiabatic flame temperature, forming a lower diffusion flame and higher LEF. When the environment pressure is high, the gas-phase combustion is dominated by the diffusion effect, larger Peclet and Damkohler numbers results in a longer diffusion flame. Under the high temperature effect of the burning surface, the gas mixture near the burning surface is easier to reach adiabatic flame temperature, forming a higher diffusion flame and lower LEF. At the same time, with the increase of Peclet and Damkohler numbers, the LEF further into the AP side and away from the oxidizer fuel interface according to the literature [30], as shown in fig. 13 (where AMF represents the AP monopropellant flame).

Conclusions

The current study is to develop a method to exactly evaluate the micro-combustion process of AP/HTPB propellant using a sandwich model. The two-step global kinetic reaction and one-step reaction represent the processes of gas cobustion and condense-phase decomposition. The predicted average burning ratesmatchwell with the experimental cases, indicating the accuracy of the proposed model.

A series of typical combustion characteristics are examined to elucidate information on multi-flame structure emanating from AP/HTPB propellant in detail. To quantitatively explain the gas phase flame structure under different environmental pressures, a method is proposed to jointly define the AP monopropellant flame height H_1, the primary diffusion flame height H_2, and the final diffusion flame height H_3 by the temperature and components distribution of the gas-phase field. Meanwhile, Peclet and Damkohler numbers are also introduced to illustrate the influence of chemical kinetics and diffusion mixing process on gas-phase combustion. Many important flame properties observed in the experiment can be replicated by this model, confirming the rationality of this approach and motivating further development.

Acknowledgment

This research is supported by National Natural Science Foundation of China No. 51176076.

References

[1] Chaturvedi, S., Dave, P. N., Solid Propellants: AP/HTPB Composite Propellants, *Arabian Journal of Chemistry*, *12* (2019), 8, pp. 2061-2068
[2] Beckstead, M. W., *et al*., Model of Composite Solid Propellant Combustion Based on Multiple Flames, *AIAA Journal*, *8* (1970), 12, pp. 2200-2207
[3] Price, E. W., *et al*., Combustion of Ammonium Perchlorate-Polymer Sandwiches, *Combustion and Flame*, *63* (1986), 3, pp. 381-413
[4] Gross, M. L., *et al*., Coupling Micro and Meso-Scale Combustion Models of AP/HTPB Propellants, *Combustion and Flame*, *160* (2013), 5, pp. 982-992
[5] Chorpening, B. T., Flame Structure and Burning Rate of Ammonium Perchlorate/Hydroxyl-Terminated Polybutadiene Propellant Sandwiches, *Proceedings of the Combustion Institute*, *28* (2000), 1, pp. 847-853
[6] Powling, J., Experiments Relating to the Combustion of Ammonium Perchlorate-Based Propellants, *Symposium (International) on Combustion*, *11* (1967), 1, pp. 447-456
[7] Brown, W. E., *et al*., An Experimental Study of Ammonium Perchlorate-Binder Sandwich Combustion in Standard and High Acceleration Environments, *Combustion Science and Technology*, *6* (1972), 4, pp. 211-222
[8] Price, E. W., Review of Sandwich Burning, *Proceedings*, 30th JANNAF Combustion Subcommittee Meeting, Naval Postgraduate School, Monterey, Cal., USA, 1993
[9] Ramakrishna, P. A., *et al*., Sandwich Propellant Combustion: Modelling and Experimental Comparison, *Proceedings of the Combustion Institute*, *29* (2002), 2, pp. 2963-2973
[10] Boggs, T. L., Zurn, D. E., The Deflagration of Ammonium Perchlorate-Polymeric Binder Sandwich Models, *Combustion Science and Technology*, *4* (1971), 1, pp. 279-292
[11] Knott, G. M., Brewster, M. Q., Modelling the Combustion of Propellant Sandwiches, *Combustion Science and Technology*, *174* (2002), 4, pp. 61-90
[12] Jackson, T, L., *et al*., The 3-D Flames Supported by Heterogeneous Propellants, *Proceedings of the Combustion Institute*, *28* (2000), 1, pp. 895-902
[13] Knott G., *et al*., Random Packing of Heterogeneous Propellants, *AIAA*, *39* (2001), 4, pp. 678-86
[14] Massa, L., *et al*., Numerical Solution of 3-D Heterogeneous Solid Propellants, *Combustion Theory and Modelling*, *7* (2003), 3, pp. 579-602
[15] Vijay, C., *et al*., Use of X-Ray Computed Tomography for Validation of Random Packs of Composite Solid Propellants, *Propellants, Explosives*, *Pyrotechnics*, *44* (2019), 7, pp. 915-922
[16] Vijay, C., Ramakrishna, P. A.. Estimation of Burning Characteristics of AP/HTPB Composite Solid Propellant Using a Sandwich Model, *Combustion and Flame*, *217* (2020), 9, pp. 321-330
[17] Miller, R., Effects of Particle Size on Reduced Smoke Propellant Ballistics, *Proceedings*, 18th Joint Propulsion Conference, Cleveland, O., USA,1982.
[18] Ishitha, K., Ramakrishna, P. A., Studies on the Role of Iron Oxide and Copper Chromite in Solid Propellant-Combustion, *Combustion and Flame*, *161* (2014), 10, pp. 2717-2728
[19] Kubota, N., Miyazaki, S., Temperature Sensitivity of Burning Rate of Ammonium Perchlorate Propellants, *Propellants, Explosives, Pyrotechnics*, *12* (2010), 6, pp. 183-187

[20] Boggs, T. L., Deflagration Rate, Surface Structure, and Subsurface Profile of Self-Deflagrating Single Crystals of Ammonium Perchlorate, *AIAA Journal*, 8 (1970), 5, pp. 867-867
[21] Hightower, J. D., Price, E. W., Combustion of Ammonium Perchlorate, *Symposium on Combustion*, *11* (1967), 1, pp. 463-472
[22] Buckmaster, J., *et al*., Numerical Modelling of 3-D Heterogeneous Propellant Combustion, *Proceedings*, 40th Aerospace Sciences Meeting and Exhibit, Reno, Nev., USA, 2002
[23] Kumar, S. V., *et al.*, A Novel Approach to Composite Propellant Combustion Modelling with a New Heterogeneous Quasi 1-D (HeQu1-D) Framework, *Combustion and Flame*, *173* (2016), Nov., pp. 411-424
[24] Kumar, S. V., Mukunda, H. S., Aluminized Composite Propellant Combustion Modelling with Heterogeneous Quasi-1-D (HeQ1-D) Approach, *Combustion and Flame*, *19*2 (2018), June, pp. 50-70
[25] Ramakrishna, P. A., *et al*., Combustion of Sandwich Propellant at Low Pressures, *Proceedings of the Combustion Institute*, *30* (2005), 2, pp. 2097-2104
[26] Hedman, T. D., *et al*., An experimental Study of the Effects of Catalysts on an Ammonium Perchlorate Based Composite Propellant Using 5 kHz PLIF, *Combustion and Flame*, *159* (2012), 4, pp. 1748-1758
[27] Hedman, T. D., *et al*., The Effect of Polymeric Binder on Composite Propellant Flame Structure Investigated with 5 kHz OH PLIF, *Combustion and Flame*, *160* (2013), 8, pp. 1531-15
[28] Zou, X., *et al*., Investigation on the Microscale Combustion Characteristics of AP/HTPB Propellant under Wide Pressure Range, *Fuel*, *306* (2021), 121652
[29] Chorpening, B. T., Brewster, M. Q., Emission Imaging of AP/HTPB Propellant Sandwich Combustion, *Combustion Science and Technology*, *174* (2002), 4, pp. 39-60
[30] Prasad, K., Price, E. W., A Numerical Study of the Leading Edge of Laminar Diffusion Flames, *Combustion and Flam*e, *90* (1992), 2, pp. 155-173

Paper submitted: November 14, 2022
Paper revised: January 13, 2023
Paper accepted: January 14, 2023